The Cryosphere, 7, 1057–1072, 2013
www.the-cryosphere.net/7/1057/2013/
doi:10.5194/tc-7-1057-2013

The Cryosphere Open Access

Summer sea ice characteristics and morphology in the Pacific Arctic sector as observed during the CHINARE 2010 cruise

H. Xie[1], R. Lei[2], C. Ke[3], H. Wang[4], Z. Li[5], J. Zhao[6], and S. F. Ackley[1]

[1]Laboratory for Remote Sensing and Geoinformatics, University of Texas at San Antonio, Texas 78249, USA
[2]Key Laboratory for Polar Science of the State Oceanic Administration, Polar Research Institute of China, Shanghai, 200136, China
[3]School of Geographic & Oceanographic Sciences, Nanjing University, Nanjing, 210093, China
[4]Department of Earth Sciences, Zhejiang University, Hangzhou, 310027, China
[5]State Key Laboratory of Coastal and Offshore Engineering, Dalian University of Technology, Dalian, 116024, China
[6]College of Physical and Environmental Oceanography, Ocean University of China, Qindao, 266100, China

Correspondence to: H. Xie (hongjie.xie@utsa.edu)

Received: 3 May 2012 – Published in The Cryosphere Discuss.: 31 May 2012
Revised: 13 May 2013 – Accepted: 2 June 2013 – Published: 9 July 2013

Abstract. In the summer of 2010, atmosphere–ice–ocean interaction was studied aboard the icebreaker R/V *Xuelong* during the Chinese National Arctic Research Expedition (CHINARE), in the sea ice zone of the Pacific Arctic sector between 150° W and 180° W up to 88.5° N. The expedition lasted from 21 July to 28 August and comprised of ice observations and measurements along the cruise track, 8 short-term stations and one 12-day drift station. Ship-based observations of ice thickness and concentration are compared with ice thickness measured by an electromagnetic induction device (EM31) mounted off the ship's side and ice concentrations obtained from AMSR-E. It is found that the modal thickness from ship-based visual observations matches well with the modal thickness from the mounted EM31. A grid of 8 profiles of ice thickness measurements (four repeats) was conducted at the 12-day drift station in the central Arctic (∼ 86°50′ N–87°20′ N) and an average melt rate of 2 cm day^{-1}, primarily bottom melt, was found. As compared with the 2005 data from the Healy/Oden Trans-Arctic Expedition (HOTRAX) for the same sector but ∼ 20 days later (9 August to 10 September), the summer 2010 was first-year ice dominant (vs. the multi-year ice dominant in 2005), 70 % or less in mean ice concentration (vs. 90 % in 2005), and 94–114 cm in mean ice thickness (vs. 150 cm in 2005). Those changes suggest the continuation of ice thinning, less concentration, and younger ice for the summer sea ice in the sector since 2007 when a record minimum sea ice extent was observed. Overall, the measurements provide a valuable dataset of sea ice morphological properties over the Arctic Pacific Sector in summer 2010 and can be used as a benchmark for measurements of future changes.

1 Introduction

The Arctic sea ice cover has been observed shrinking in area and thinning during the past three decades (Serreze et al., 2007; Stroeve et al., 2007; Comiso et al., 2008, Perovich, 2011). Its first-year ice (FYI) has replaced much of the multiyear ice (MYI) (Kwok and Rothrock, 2009; Maslanik et al., 2007; Nghiem et al., 2007). The more than 11 % per decade (in recent 3 decades) in decline in September ice extent (Perovich, 2011) is far larger than the prediction of modeling results (Intergovernmental Panel on Climate Change (IPCC), 2007). Summer ice extent in 2007 through 2012 has been lower than during any other year since the start of the satellite record in 1979, with a new record minimum set in 2012. The most significant decline of ice extent was between 150° W and 120° E including the Chukchi and East Siberian Seas. From spaceborne measurements, ice concentration in summer seasons decreased from primarily 90 % over the central Arctic in the 1978–2000 period to less than half of the region at 90 % in the 2003–2008 period (Kwok and Rothrock, 2009). Ice thickness is technically more difficult to measure

from space. However, the combined submarine and ICESat records show that the average ice thickness of the central Arctic in fall has decreased from 3.0 m (1958–1976) to 1.4 m (2003–2007) (Kwok and Rothrock, 2009), a 53 % decrease in about 40 yr. The rate of decline appears to be much higher in recent years. Helicopter electromagnetic (EM) measurements in the Arctic North Pole region (central Arctic ocean) found that the mean sea ice thickness decreased from 2.2 m in 2001 to 1.3 m in 2007 (Haas et al., 2008), a 41 % decrease in 6 yr. Haas et al. (2008) called summer 2007 the regime shift for the Arctic North Pole region from multi- and second-year ice dominant to first-year and younger ice dominant and this shift had remained in 2009 (Haas et al., 2010). Recent work in the eastern Arctic (30 to 130° E, 82 to 89° N) in summer 2012 confirmed from airborne EM measurements that first-year ice also dominated (> 95 %) in that region (Boetius et al., 2013).

The decommissioning of ICESat in 2009, coupled with the delayed launch of ICESat2 in 2016, suggests there will be a significant gap in the high resolution ice thickness record. The launch of CryoSat in April 2010 may provide significant altimetric data to fill the gap. During Arctic summer however, the ice or snow surface is rather wet, characterized by numerous and spatially extensive melt ponds (Lu et al., 2010; Perovich, et al., 2008, 2009; Eicken et al., 2004). This wet ice or snow surface likely causes large errors in the CryoSat estimates of ice thickness (Haas and Druckenmiller, 2009). Ship-based and airborne observations provide some alternative methods to discern regional-scale changes in ice thickness in summer seasons from 2009 and may assist in CryoSat validation until 2016 when ICESat-2 data are planned to become available.

The Chinese National Arctic Research Expedition (CHINARE) from 1 July to 20 September, 2010, conducted multi-disciplinary scientific studies on atmosphere–ice–ocean interactions and the marine ecosystem's response to climatic change in the Arctic Pacific Sector, based on icebreaker R/V *Xuelong*. The sea ice team collected a comprehensive dataset on sea ice morphological and physical properties of the sector, in particular between 150° W to 180° W up to 88.5° N, from 21 July to 28 August.

The first objective of the paper is to present our results based primarily on (1) underway visual observations of sea ice at half-hourly intervals and (2) on-ice measurements of snow and ice thickness using an electromagnetic induction instrument, the Geonics EM31 (9.8 kHz), at one 12-day and eight short-term (3–4 h each) ice stations. The second objective is to compare the visually observed ice thicknesses with those from the EM31 mounted off the ship's left side, at a height of 3.5 m above waterline and 8 m from the ship (Wang et al., 2012). The third objective is to compare the visually observed ice concentrations with the corresponding AMSR-E ice concentrations. The fourth objective is to compare the sea ice condition in 2010 with the HOTRAX05 (Healy/Oden Trans-Arctic Expedition 2005) results.

A previous comparison for the Arctic Pacific Sector between the HOTRAX05 and the AOS94 (Arctic Ocean Section 1994) expeditions showed overall reduced ice concentration for the 70–80° N latitudes and increased pond coverage for the 75–80° N latitudes, while the ice concentration and pond coverage did not show much change for other latitude degrees (above 80° N for concentration and pond coverage and below 75° N for pond coverage) (Perovich et al., 2009). Results from this 2010 cruise are compared with the HOTRAX05 to extend this comparison beyond 2007.

2 Study area and methods

Figure 1 shows the cruise track and ship-based observations of sea ice and ice stations, primarily in the Chukchi Sea, Beaufort Sea, Canada Basin and Central Arctic Ocean. The underway ship-based ice observations are divided into 3 legs, the westward, northward, and southward legs for clearer discussions later in the paper. The observations were conducted from the ship's bridge, on a half-hourly basis. The observation protocol, similar to the Antarctic Sea ice Processes and Climate (ASPeCt) protocol (Worby and Allison, 1999; Worby et al., 2008), was used to record the principal information related to ice concentration, floe size, ice type, melt pond coverage, and ice and snow thickness. In the presence of several different ice types, ice type, floe size, concentration, and thickness were recorded separately for each ice type. In this paper, ice concentration, floe size, melt pond coverage, and ice thickness of the dominant ice type (i.e., the highest ice concentration) are presented. The observed ice concentration is also compared with the AMSR-E ice concentration, 12.5 km in cell size from the National Snow and Ice Data Center (NSIDC), for validation purposes.

A Geonics EM31-ICE (9.8 kHz) was mounted off the ship's left side, at a height of $\sim$3.5 m above waterline and 8 m from the ship, with a data collection rate of 1Hz (Wang et al., 2012). The precise distance from the instrument to the surface (water, snow, or ice) was measured with an ultrasonic ranger (D_S) and a laser altimeter (D_L) attached to the EM 31 carriage. The distance from the EM device to water or the interface between ice bottom and water (D_{EM}) was the direct output from the EM31-ICE (seawater conductivity 2500 m S m^{-1} was used). Using paired readings (D_{EM} and D_S) during 8 periods when ship was sailing over relatively calm open water areas and treating the D_S as the true distance, a linear regression equation to convert the D_{EM} values to calibrated (true) value (D'_{EM}) is then determined as Eq. (1)

$$D'_{EM} = 0.938 \times D_{EM} + 0.001, \quad (R^2 = 0.99). \tag{1}$$

The D_S or D_L is then subtracted from $D'_{EM}$to derive a combined snow and ice thickness (T) for each data collection. In most cases, the D_L is used to calculate the T. But for

Fig. 1. Ship tracks of half-hourly visual observations of sea ice for the three (westward, northward, and southward) legs, with ice station (IS) location and identification (number and date (MMDD)); LIS denotes the 12-day ice station from 7 August to 19 August. Other information included are date and location of ice seen first (21 July) and last (28 August), ice extent of 24 July and 28 August from AMSR-E ice concentration data, and HOTRAX 2005 ship track (9 August to 10 September, northward) with ice observations in the similar area (courtesy of D. Perovich).

cases when D_L values varied a lot due to the instrument shaking or no D_L values due to laser pointing over water, D_S is then used to calculate the T. More details about the calibration and operation of the EM 31 were described elsewhere (Weissling et al., 2011). The instrument started collecting data on 1 August (around 79.5° N) and ended on 28 August (around 75° N).

One 12-day and eight short-term (3–4 h each) ice stations (Fig. 1) were conducted during the cruise, with detailed snow, ice, and pond physical properties measured and sampled. The second Geonics EM31 instrument (9.8 kHz) was used for snow and ice thickness measurements along designed profiles in each ice station. A total of 31 profiles and 2957 sampling points were performed (Table 1). The EM31 was hand-carried by the same operator at roughly the same height above the surface (0.85 m) collecting data (discrete sampling) in vertical dipole mode (see photo IS3 of Fig. 2). At each sampling point, in order to compensate for the thickness heterogeneity of sea ice in different directions, two data samples were recorded, one with the instrument's longitudinal direction parallel to the walk direction and the other with the instrument's longitudinal direction perpendicular to the walk direction. The mean conductivity (C in m S m^{-1}) of the two readings at one point is counted as one discrete sample reading. The empirical equation (2) (courtesy of B. Weissling), derived over level first-year ice from a previous field campaign (2008) near Barrow, Alaska using the same EM31 unit, was used to convert the measured conductivity (C) to height.

$$\text{height (m)} = 13.1509 - 1.9246 \times \text{LN}(C) \quad (2)$$

The EM-estimated thicknesses (m), height − 0.85 (instrument height) + depth stepping into snow cover (m), were compared with borehole-drilling thicknesses (along the profile lines 1 and 2 in work zone 2) with good agreement (3–7 % error).

To better describe the changes in terms of ice thickness, ice type, ice concentration, floe size, and pond coverage along the cruise tracks, we separate them into two different zones: the marginal ice zone (MIZ) and the pack ice zone. MIZ is the ice area where open ocean processes (mostly waves and swells) significantly change the dynamical properties of sea ice cover (Squire, 2007; Leppäranta, 2005). There is usually

Table 1. EM 31 profiles and sampling points in each station.

Ice stations	Profiles	Points	Comments
IS-1 (27 July)	1	88	Short profile (1 m interval)
IS-2 (30 July)	4	161	Short profiles (1 m interval)
IS-3 (1 Aug)	3	167	Short profiles (1 m interval)
IS-4 (3 Aug)	5	118	Short profiles around two melting ponds (1 m interval)
IS-5 (5 Aug)	4	226	Short profiles (1 m interval)
	1	230	One circle covering the entire floe (continuous mode)
LIS (7–19 Aug)	8 (work zone 2)	640 (160 × 4)	Four repeats for the 8 profiles (5 m interval)
	2 (work zone 3)	390 (130 × 3)	Three repeats for the 2 profiles (2.5 m interval)
IS-6 (20 Aug)	1	239	One circle covering the entire floe (continuous mode)
IS-7 (23 Aug)	1	138	One circle covering the entire work zone (1 m interval)
IS-8 (24 Aug)	1	409	One circle covering the entire floe (continuous mode)
Total	31	2957	

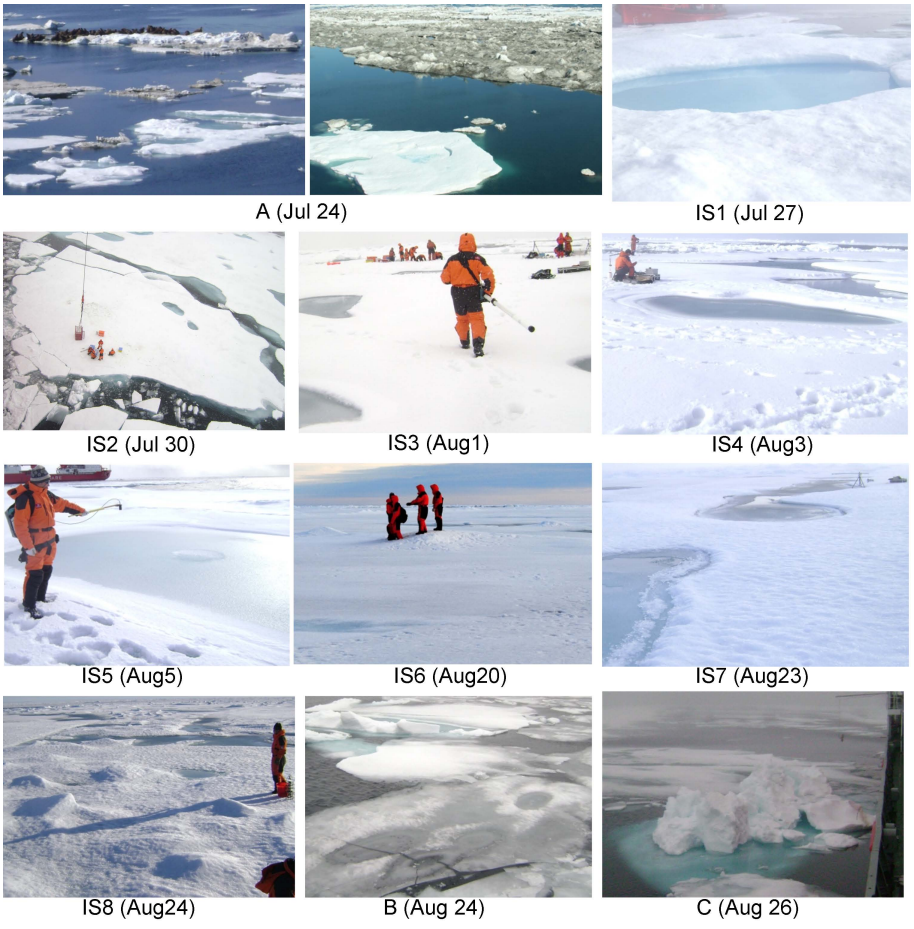

Fig. 2. Photos of typical snow and ice taken from the ship or on the eight short-term ice stations (IS1 to IS8) from the 2010 cruise. **(A)** dirty ice in the marginal ice zone, left photo: hundreds of walruses were seen over dirty ice; right photo: a floe size of 500 m dirty ice with rough surface of up to 2 m in thickness; (IS1) loose granular sea ice layer of depth 2–8 cm, blue color pond, with Huanghe (red boat) on top left; (IS2) loose granular sea ice layer of depth 2–8 cm; (IS3) new snow of 5–6 cm on top, a mean depth of 13 cm with a loose granular sea ice layer below new snow; (IS4) new snow on top, a mean depth of 15 cm with loose granular sea ice layer below the new snow; (IS5) new snow on top, a mean depth of 15 cm; (IS6) refrozen granular sea ice layer snow (firn-like), mean depth of 10 cm; (IS7) refrozen granular sea ice layer l (firn-like), mean depth of 10 cm; (IS8) refrozen granular sea ice layer (firn-like), a mean depth of 10 cm; **(B)** thin new ice and old thicker ice with blue melt ponds; **(C)** floeberg of 10 m in diameter and over 4 m above the sea surface, hit by the hanging EM31 (up right corner).

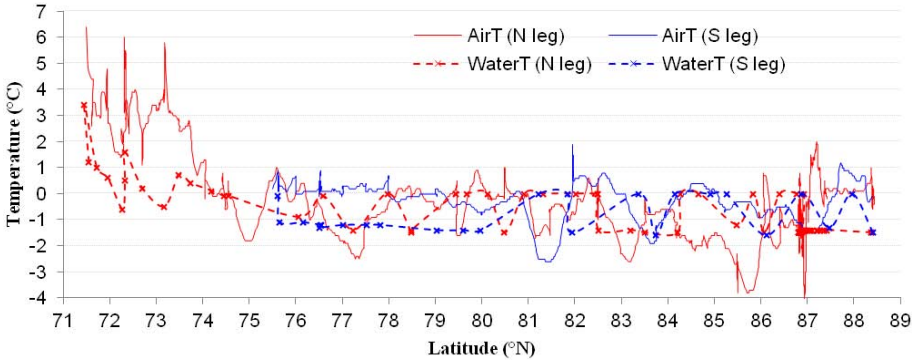

Fig. 3. Ship-based air (solid lines) and water (dashed lines) temperatures for northward leg (red, 25 July–20 August) and southward leg (blue, 20–28 August) during the CHINARE-2010. The air temperature was continuously measured and the water temperature measurement was interrupted once the ship was moving in the ice. For detailed timing and locations of ice stations refer to Figs. 1 and 5a.

a distinguishable increase in floe size and ice concentration in traversing from the MIZ into the pack ice zone.

3 Overview of sea ice and weather conditions during the cruise period

During the cruise, ice was first seen at 69.80° N,168.97° W, on 21 July, in the Chukchi Sea, and last seen at 75.61° N,172.16° W, on 28 August (Fig. 1). It therefore retreated about 650 km over the 38-day period from 21 July to 28 August. Representative ice extents from two AMSR-E ice concentration datasets (24 July and 28 August) are also shown in Fig. 1 as background. It is interesting to see that the southernmost location of ice seen on 21 July (also in the AMSR-E map on 21 July, not shown) was still the southernmost location of ice mapped by the AMSR-E on 24 July. This suggests that, south of this position, ice could not survive any more in the late July period due to the warmer water and air temperature. The westward leg was well situated in the MIZ of 24 July AMSR-E mapped ice extent. However, the AMSR-E ice extent of 28 August was ∼ 23 km south of the last observed ice location. This difference of two AMSR-E pixels on 28 August could be due to slight differences between the observation and the imaging time, i.e., the imaging time was slightly earlier than the observation time on the surface. Overall, however, the AMSR-E ice extents (edges) matched reasonably well with the visually observed ice edges in the study period.

During the entire cruise period, ice was in a stage of rapid melting and retreating, while some precipitation events modified the melt, with at least two moderate snowfall events from 31 July to 4 August, two additional small snowfall events from 7–11 August, one rainfall event on 17 August, and several rainfall events from 26–28 August. With a few exceptions (Fig. 3), the air and water temperatures were generally above 0 °C south of 74.5° N (prior to 29 July), while between −1.5 °C and 0 °C north of 75° N. All the snowfall events occurred when the air temperature was at or below −2 °C. Obvious freeze-up was seen on 24 August (Fig. 2) when air temperature was below −2 °C between 82–81 ° N during the southward leg (Fig. 3). Water temperature north of 75° N was generally between 0 °C to −1.5 °C, which was not low enough for sea water to freeze. Therefore, the freeze-up mostly occurred due to the fresher melt water inside the melt ponds during the cruise period. The rainfall event during the 12-day ice station (northward leg) was related to the warm spike (at 87.2–87.3° N) up to 1.9 °C on 17 August (Fig. 3), which resulted in distinct snowmelt occurring over the ice surface and a decrease in surface albedo (Lei et al., 2012). While the ship was in the ice, most of the time the weather was either foggy or with overcast skies or both. Sunny skies or partly cloudy skies were observed on only a few days.

4 Results

4.1 Visual observations of snow and ice properties

4.1.1 Westward leg

As shown in Fig. 1, the westward leg was short (∼ 280 km) and was entirely within the marginal ice zone (MIZ) less than 50 km south to the ice edge, from 24 July (10:00 UTC) to 25th (06:30 UTC). Ship speed was 6–8 kts. Salinity of the surface water (based on measurements by an underway continuous flow system of R/V *Xuelong*) along this leg was about 26 psu. This indicates that the sea ice was in the melting process which reduced the salinity of sea water at the surface. Ice concentration (IC) in the first half of the leg was 40 % or less, increased to 60–90 %, and decreased again in the last 40 km before exiting the ice zone, a similar pattern was seen from both visual observations and AMSR-E (Fig. 4a). Melt pond coverage (MC, i.e., pond-covered ice) was between 0 to 30 % of ice with a mean of 10 %. Floe size was less than 20 m for the first half of the leg, increased to between 20–100 m, and then to 100–500 m, and decreased again to less than 20 m in

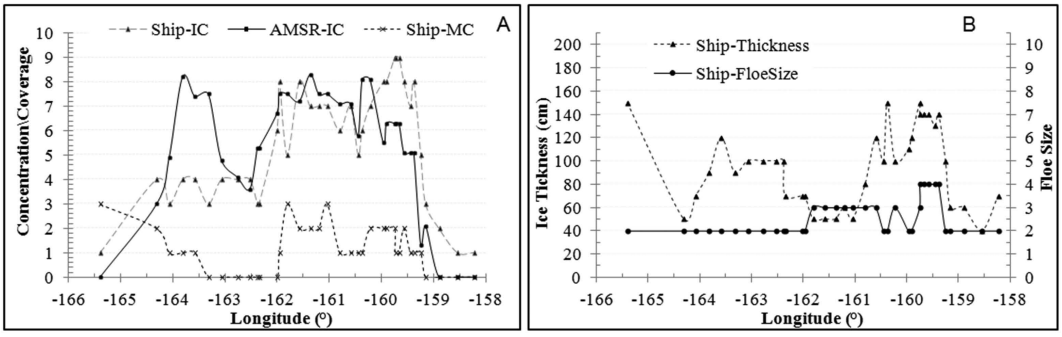

Fig. 4. Ship-based visual observations of sea ice thickness, floe size, melt pond coverage (MC), and concentration (IC), and AMSR-E ice concentration for the westward leg of the CHINARE-2010 cruise, from 24 July, 10:00 UTC to 25 July, 06:30 UTC. Floe size code: 1 (< 2 m), 2 (2–20 m), 3 (20–100 m), 4 (100–500 m), 5 (500–2000 m), 6 (2–10 km), and 7 (> 10 km). Ship traveled westward in the marginal ice zone of 280 km or ∼ 40 km per longitude degree.

the last 40 km before exiting the ice zone (Fig. 4b). Ice thickness was between 40 to 150 cm; a relatively loose surface layer of granular decomposing sea ice (Perovich et al., 2002, 2003), which was first mislabeled as a snow layer and was later corrected, was less than 10 cm; Ice type was primarily first-year ice, with level ice dominant and ridged areas accounting for 5–10 % of the ice area. Some small isolated floebergs (20–40 m), with 2–5 m elevation above sea level, were also seen. These were pieces of highly ridged, perhaps multiyear, ice. Besides those clean/white ice types, dirty ice, brownish, many holes inside, with large roughness was found as well (Fig. 2a). Dirty ice may have formed due to sediment entrainment in coastal regions, either through anchor ice or suspension freezing (Darby et al., 2011; Eicken et al., 2005; Kempema et al., 1989). The fraction of dirty ice ranged from 1–5 % in the central sector of the leg and 10–15 % (can be up to 70–80 %) near ice edges of the leg. The relatively low albedo of dirty ice introduced a high melt over ice surfaces and resulted in a high surface roughness.

4.1.2 Northward and southward legs

The northward leg started near Barrow, Alaska at 71.35° N,156.94° W, on 25 July, and ended at 88.36° N,177.52° W, on 20 August. One 12-day and six short-term (3-4 hours each) ice stations were conducted along the northward leg. The southward leg started on 20 August and ended (out from the ice zone) on 28 August. Two short-term ice stations were conducted along this leg. The ice observation results of dominant ice type (highest ice concentration) are included in Fig. 5a–c.

The region south of 75° N along the northward leg (Fig. 5_A1) and south of 80° N along the southward leg (Fig. 5_A2) can be defined as MIZ. The clear boundary between the MIZ and pack ice zone is where the ice concentration immediately drops below 60 % (in the MIZ) and stays below 50–60 % on a more or less continuous basis out to the open water. In the MIZ, ice concentration was still highly variable from 0 to 90 % but with a mean of 30 % (from a total 88 observations in the northward leg and 66 in the southward leg). In the pack ice zone, the concentration was overall larger than 50 % nearly continuously, with a mean of 66 % (272 observations) for the northward leg and 71 % (179 observations) for the southward leg.

Based on visually observed ice concentrations and AMSR-E ice concentrations (Fig. 5a), the overall patterns of lower concentration in the MIZ and higher concentration in the pack ice from the two datasets reasonably match, although the AMSR-E ice concentrations were overall higher than visually observed in the pack ice zone and lower than visually observed in the MIZ, resulting in an R^2 of only 0.53 for the entire cruise (not shown). The latitudinal extents of the MIZ, however, from both surface-based and satellite datasets were clearly comparable and were quite the same: 71.5–75° N (∼ 350 km) for the northward leg (from 25–30 July) and 75.5–80° N (∼ 450 km) for the southward leg (from 25–28 August). This agreement suggests that daily AMSR-E ice concentration data might be used to approximately map the MIZ and its changes.

Melt pond coverage (MC) varied differently in the MIZ and pack ice zones, with overall similarities within the MIZ or pack ice zone along the two legs (Fig. 5a). First, the MC was overall lower in the MIZ than in the pack ice zone, i.e., 16 % vs 23 % for the northward leg and 10 % vs 33 % for the southward leg; second, in the pack ice zone, the MC shows an overall decreasing trend northward (i.e., from lower latitude to higher latitude), and it is even more obvious in the southward leg. The MC was up to 70 % around 81° N (southward leg), on 24 August, where dominant ice (80 % of the ice) had thicknesses from 50–80 cm (Fig. 5b). Melt ponds were in a status of almost melted through (Fig. 2b), which left many new thin (10–30 cm) ice lenses (formed on the surface of refrozen melt ponds) floating everywhere. The other ∼ 20 % of the ice here, about 1.5 m in thickness, was still thick old ice, with a ridged area of 30 % and blue color ponds, indicating blue ice below (second-year or multi-year ice) (Fig. 2b).

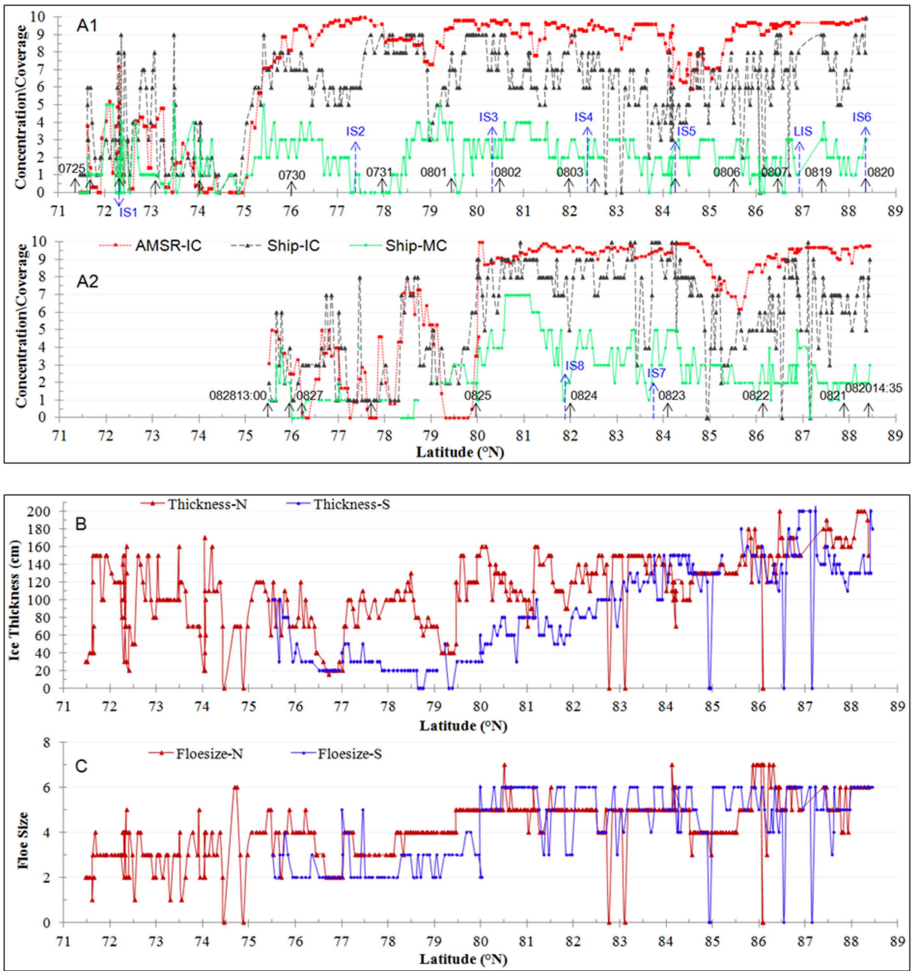

Fig. 5. Ship-based visual observations of sea ice thickness, floe size, melt pond coverage (MC), and concentration (IC), and AMSR-E ice concentration during the CHINARE-2010, from 25 July–20 August (northward leg, **A1, B, C**), and 20–28 August (southward leg, **A2, B, C**). Location of ice stations (IS1 to IS8) and date (with time) are also marked in A1 and A2; MIZ is south of 75° N in A1 and south of 80° N in **(A2)**. Floe size code: 1 (< 2 m), 2 (2–20 m), 3 (20–100 m), 4 (100–500 m), 5 (500–2000 m), 6 (2–10 km), and 7 (> 10 km). It is about 100 km per latitude degree.

Ice thickness and floe size also show obvious differences between the MIZ and the pack ice zone (Fig. 5c, c). In the MIZ, ice thickness was ∼100 cm in late July (northward leg) and thinned to less than 50 cm in late August (southward leg), while floe size was typically 2 to 100 m. In the pack ice zone, however, floe size of the dominant ice type was between 500 m to 10 km; ice thickness had an overall latitudinal trend of increase northward (or decrease southward). The decreasing trend of ice thickness was more dramatic in the southward leg (Fig. 5b), indicating both bottom and surface melting was more widespread in late August. For the northward leg, the majority of ice thicknesses were between 100 to 150 cm, with mean 114 ± 39 cm and median 120 cm for the entire leg, and mean 119 ± 37 cm and median 120 cm for the pack ice zone alone (not shown). For the southward leg, it shows two peak thicknesses (Fig. 6d): 30 cm, mostly in the MIZ where significant melt occurred into late August, and 130 cm, mostly in the high latitude area, with mean 101 ± 56 cm and median 125 cm for the entire leg, and mean 120 ± 38 cm and median 130 cm for the pack ice zone alone (not shown). None of these two thickness distributions (northward and southward) shows a single peak with long tail to right, which is a common ice thickness distribution from other means such as field measurements and remote sensing (Haas et al., 2008; Wang et al., 2013; Weissling et al., 2011; Xie et al., 2011, 2013; Zwally et al., 2008). This behavior indicates that the visual observation of ice thickness (even at the half hourly rate) is still very selective of the level ice thickness and probably undersamples thicker ice. One major reason is that visually observed ice thickness is derived by measuring the thickness of the upturned ice blocks adjacent to the ship's hull against a scale fixed above the water line, while thicker and ridged ice is usually broken apart during overturning (Toyota et al., 2004; Xie et al., 2011).

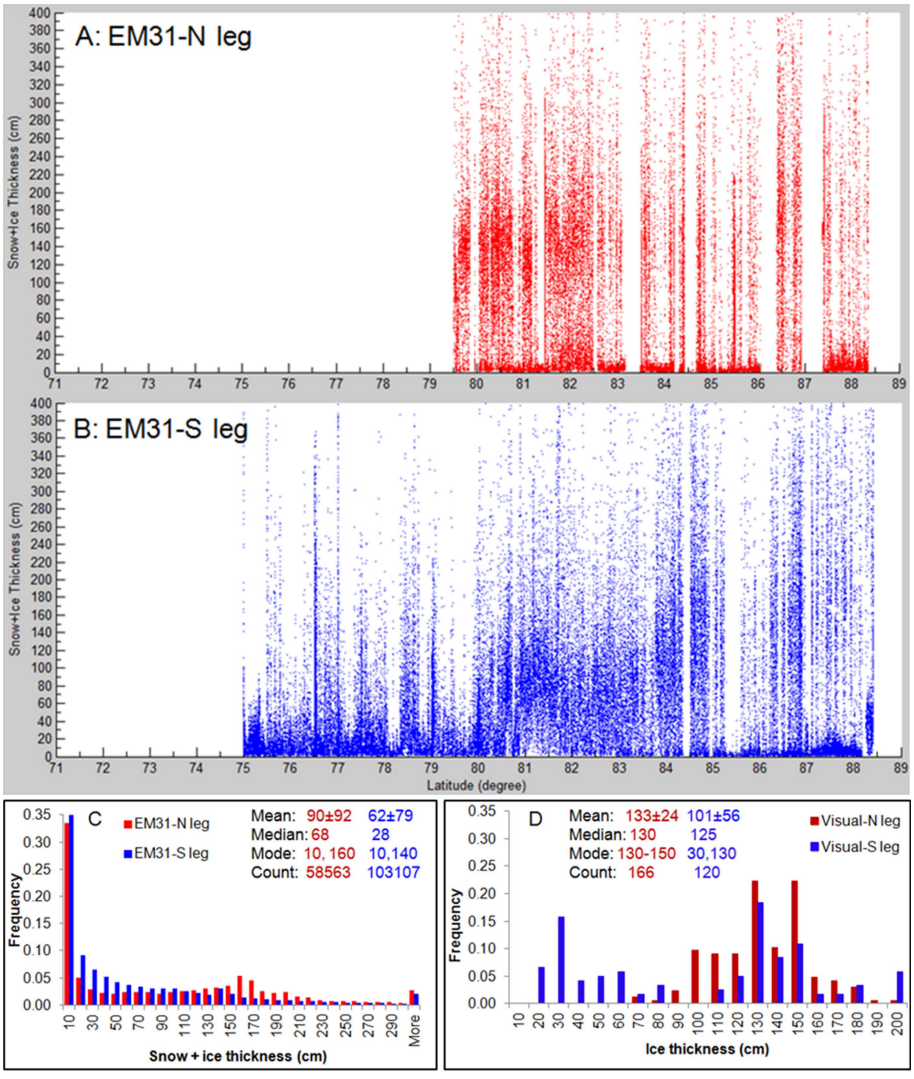

Fig. 6. EM31-derived snow and ice thickness for the northward leg **(A)** and southward leg **(B)**, with distributions **(C)**. The corresponding ice thickness distributions from visual observations for the same period for northward and southward legs shown in **(D)**.

4.2 Ice thickness comparison between visual observations and EM31 measurements

Figure 6 shows the snow and ice thickness measured from the EM31 mounted off the ship's left side. Both distributions (northward leg and southward leg) show two peaks (Fig. 6c), with a long tail to the right (maximum thickness 626 cm for the northward leg and 902 cm for the southward leg, not shown). The 10 cm modal thickness of both legs should be from the water surface, the second mode should correspond to dominant level ice of each leg, i.e., 160 cm for the northward leg and 140 cm for the southward leg. This matches well with the corresponding largest modal thicknesses from visual observations during the same period, i.e., 150 cm for the northward leg and 130 cm for the southward leg (Fig. 6d). The southward leg also includes a modal thickness of 30 cm, which was primarily due to the extensive melt that occurred in the MIZ and is shown in both EM31 (Fig. 6b) and visual observations (Fig. 5b).

4.3 Ice thickness distributions from the eight short-term ice stations

Figure 7 shows the snow and ice thickness distribution and basic statistics measured by EM31 from the 8 short-term ice stations. The IS1 and IS2 show the highest mean, median, and modal ice thicknesses. The IS1 was in the MIZ (see Figs. 1 and 5_A1) from overall thicker first-year ice or second-/multi-year ice, while the floe size is 100 m or less. The ice floe of IS2 was just off the ship (see a photo in Fig. 2). The measured ice thickness for this floe might have been contaminated by small floes submerged under the measured floe when the ship broke through the ice and parked on or next to

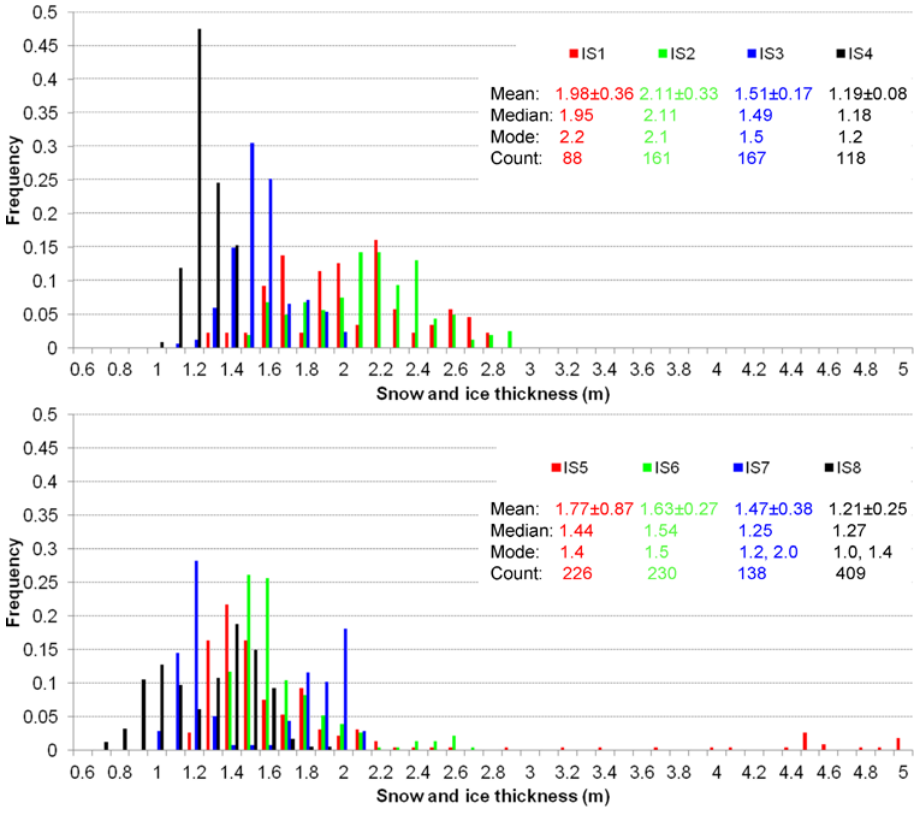

Fig. 7. EM31-measured snow and ice thickness distributions and statistics from the 8 short-term ice stations of the 2010 cruise.

the floe. IS3-5 were all conducted after or during two snowfall events that occurred in the area, adding ∼ 6 cm new snow to IS3, and ∼ 8 cm to IS4 and IS5. Walking with the carried EM31 on such new/loose snow surface, it was easy to step into snow (Fig. 2) sinking to a depth of about 6–9 cm. IS5 was an ice floe over 300 m in diameter. Some measurements conducted over ice ridges of the floe show up to 5 m in thickness. IS6 (20 August) was the northernmost station conducted in the cruise and was one day after the 12-day drift station and 3 days after a slight rainfall event (on 17 August). The rainfall and higher temperature caused new snow to completely melt away from the top of the granular decomposing ice. Both IS7 and IS8 were conducted during the southward leg, both showing a two-peak thickness distribution, with granular decomposing ice of 0.1 m on the top. The thinner peak (1.2 m for the IS7 and 1.0 m for IS8) was overall flat ice and/or ice closer to melt ponds, while the thicker peak (2.0 for IS7 and 1.4 m for IS8) was overall ridged ice. Overall, the 8 short-term stations provide ice thickness distributions only for samples of ice floes along the ship tracks but match well with overall thickness distributions from both the ship-mounted EM31 and visually observed ice thickness along the cruise.

4.4 Ice thickness distribution and change from the 12-day (drift) ice station

The 12-day ice station from 7–19 August as shown in Fig. 8 was on a more than 10 km by 10 km floe of multiyear ice, with average melt pond coverage of 30 % and mean ice thickness of around 1.8 m. Although it was claimed as first-year ice in Lei et al. (2012), we would argue that it was most likely multiyear, based on (1) it was a large floe with 30 % of highly organized pond patterns (Eicken et al., 2004; Perovich et al., 2009) and highly variable ice thickness along horizontal transects/profiles (see Fig. 9), (2) it had coarse grained columnar ice at the very top (see in Lei et al., 2012), (3) it had at least 2 m in thickness before the summer melt, and (4) near-zero salinity down to 0.5 m or more (see in Lei et al., 2012). Figure 8c shows the overall thinning from a mean 1.89 m (10 August) to 1.71 m (19 August) in zone 2, and from 1.76 m (11 August) to 1.60 m (18 August) in zone 3, i.e., a mean thinning of about 2 cm day^{-1} for zone 2 and 2.5 cm day^{-1} for zone 3. Surface melt during the station period was not observed until the last two days, and thus the bottom melt was the main reason for the thinning in this period (Lei et al., 2012).

Figure 9 shows examples of thickness measurements and changes for zone 2 (four repeats) and zone 3 (three repeats). It is clear that the sea ice thickness varied, i.e., thicker when

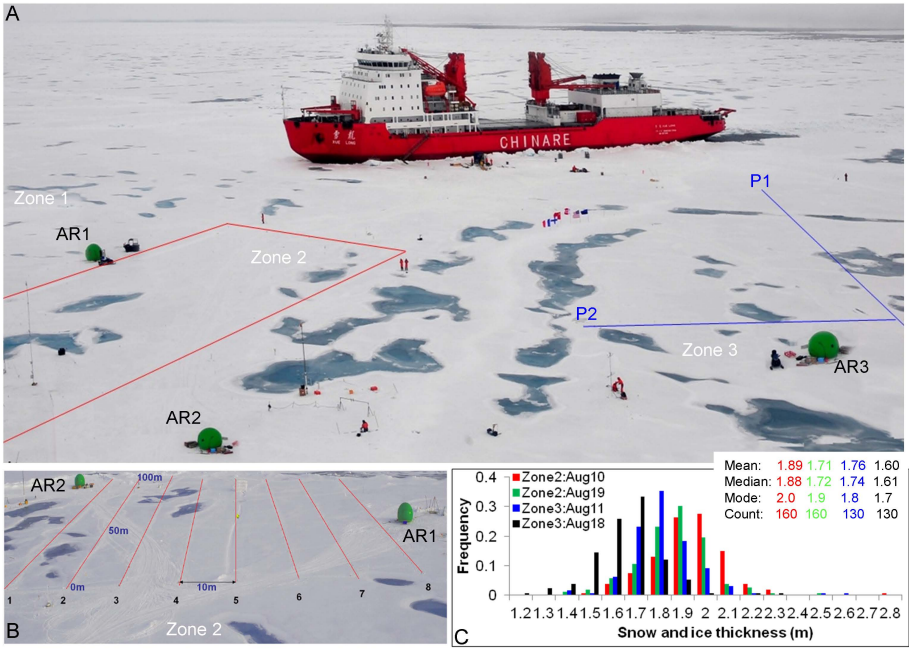

Fig. 8. The 12-day drift station (7–19 August) over the multiyear ice floe of more than 10 km × 10 km **(A)**, with R/V *Xuelong* in the back, and three work zones and three apple rooms (AR) marked; A grid of 8 profiles (100 m long and 10 m apart) in zone 2 **(B)** and two profiles (200 m for P1 and 125 m for P2) in zone 3 used for repeated sea ice thickness measurements using the EM31; Sea ice thickness distribution and basic statistics from the first and last measurements over zone2 and zone3 **(C)**. A crack (whiter or higher albedo than surrounding) along and crossing the line 5 in work zone 2 is clearly seen in **(B)**.

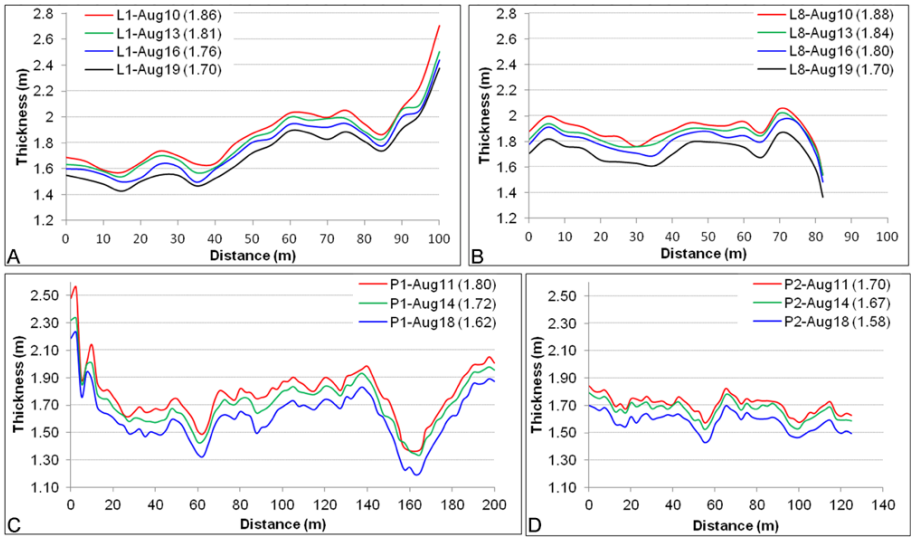

Fig. 9. Examples of repeated EM31 snow and ice thickness measurements: **(A)** and **(B)** respectively for profile line 1 (L1) and line 8 (L8) in work zone 2; **(C)** and **(D)** respectively for profile P1 and P2 in work zone 3. Number in the brackets is the mean thickness of the profile measured in that day. The start points (or 0 m distance) of profiles in Zone 2 were marked in Fig. 8b; the start point of P2 was the intersection point of P2 and P1, while the start point of P1 was out of the Fig. 8a, to the lower right corner.

closer to ridges (the locations at 100 m of profile L1 and 0 m of profile P1) and thinner when closer to large melt ponds (the location at 160 m of profile P1) or open leads (the location at 82 m of profile L8). Those locations also refer to Fig. 8. All other small valleys in the profiles were associated with small melt ponds nearby. This indicates that melt ponds (and open leads) not only can accelerate the surface melt but also accelerate the bottom and bottom's nearby melt

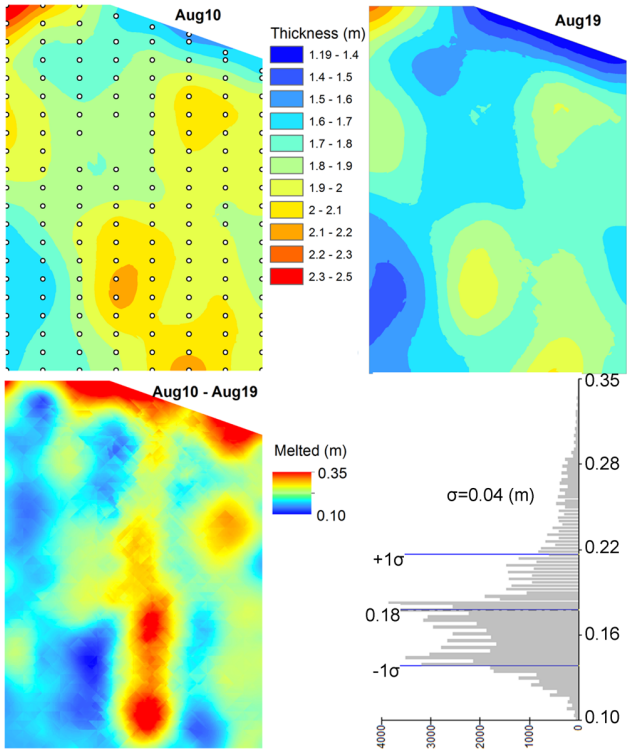

Fig. 10. Snow and ice thickness maps of 10 August, 19 August, difference map (or melted ice) between 10 August and 19 August, and frequency distribution of the difference map (mean 0.18 m and standard deviation of 0.04 m). The small circles on the 10 August map show the locations of individual EM31 measurements (5 m apart along the profiles and 10 m apart between profiles).

of ponds, since more solar radiation penetrates through the water and/or thinner ice and is used for bottom melt under or nearby these ponds or leads. There is also general bottom melt due to heated (or warmer) ocean water underneath moving ice forced by ocean currents and winds. This is seen as the consistent and general thinning everywhere along each profile. The thickness differences between the last two measurements for all profiles were always slightly larger than the differences between any two earlier measurements for the same profile. This is consistent with our observations that there was some surface melting on the 18th and 19th due to a rainfall event on the 17th and overall higher air temperature (larger than 0 °C) on the 17th and 18th (Fig. 3).

The point measurements of snow and ice thickness based on the EM31 over the 8-profile grid in one day (one repeat) can be used to produce a thickness map showing the spatial distribution of ice thickness (as shown in Fig. 10). Geostatistical approach, here the ordinary Kriging method, is used to produce the thickness map. Figure 10 shows a similar pattern of spatial thickness distributions for the first (10 August) and last (19 August) repeats. The thicker ice was in the upper left corner (ridge) and lower right portion of the area (no melt ponds), while the thinner ice was primarily in upper right (next to large open leads) and lower left (multiple melt ponds) portions of the area. The largest thickness changes (melt) occurred (1) along the top edge (ridge on the top left and open leads on the top right) and (2) new opening crack along or crossing profile 5 (the crack clearly seen in the Fig. 8b). The opening crack was narrower than 20 cm and almost covered by new snow (higher albedo) in the first five days, and gradually widened to 50 cm or more in some local portions by the end of the station period. The opening crack introduced more solar radiation to melt the ice (both lateral and bottom melts). It is also clear that, even along the opening crack from top edge to bottom edge of Fig. 10, the melt rate was quite different. The melt rate was lower in the top half (not including the very top part where it was very close to the wide open water) than in the bottom half, although the ice was generally thinner in the top half than in the bottom half. This might be due to higher levels of solar radiation with crack widening downwards in the bottom half. A measured melt rate under ridged ice (top left) is consistent with the SHEBA experiment results that the deformed ice showed a larger bottom melt rate than undeformed ice (Perovich et al., 2003). The ablation distribution plot (Fig. 10) shows a central peak range (0.14–0.19 m), with a mean of 0.18 m (±0.04 m), minimum of 0.10 m, and maximum of 0.35 m, i.e., a mean thinning of about 2 cm day^{-1} for work zone 2 area.

5 Discussion

5.1 A comparison between HOTRAX-2005 and the CHINARE-2010 cruises

Compared with ice observations of HOTRAX05 (cruise track also included in Fig. 1) (Perovich et al., 2009), there were obvious differences between 2005 and 2010, in terms of ice type, concentration, thickness, snow cover, and melt pond coverage. Overall, after the first record low of 2007 summer minimum ice extent in the Arctic ocean (Comiso et al., 2008; Simmonds and Keay, 2009), the ice situation in the Arctic Pacific Sector seems to have continued. In 2005, multiyear ice was the dominant ice type with ice concentration of 80–100 % north of 79° N; in 2010, however, the dominant ice type was first-year ice, with lower mean ice concentration in the pack ice zone 66 % for the northward leg (north of 75° N) and 71 % for the southward leg (north of 80° N), even less if ice in the MIZ is included. In 2005, the mean ice thickness was ∼ 150 cm from 9 August (76° N) to 10 September (88.72° N); in 2010, however, the mean ice thickness was 114 cm for the northward leg and 94 cm for the southward leg (including the MIZ, or ∼ 120 cm for the pack ice zone alone). In 2005, the pond coverage showed a clear latitudinal decrease with a mean of 35 %; in 2010, a similar latitudinal trend was also shown in the pack ice zones, while the latitudinal trend is clearer in the southward leg than that in the northward leg, and the mean pond coverage was 25 %

for the entire period. In 2005, no snow was found on sea ice up to 84.3° N (29 August 2005) and about ∼ 10 cm thereafter; in 2010, besides a similar decomposed granular sea ice layer (less than 10 cm) seen throughout the ice zone, several snowfall events (since 31 July) added ∼ 8 cm new snow on top of the decomposed granular sea ice layer seen from 78–87.5° N; the new snow was then melted away due to a rainfall event on 17 August. In the North Pole region, during the helicopter-based electromagnetic measurements of 2001, 2004, and 2007, no snow cover was observed in August and 10 cm new snow seen in September (Haas et al., 2008; Rabenstein et al., 2010).

The ice thinning in 2010 as compared with 2005 provides additional information to support the significant ice thinning from the submarine period (1958–1976) to ICESat period (2003–2008) (Kwok, 2011; Kwok and Untersteiner, 2011) for the Pacific Arctic Sector and air-borne EM31 based ice thickness measurements from 2001 to 2009 for the Central Arctic (Haas et al., 2008, 2010).

It is not clear why the pond coverage seems to decrease as compared with the 2005 data, although one possible reason might be related to the multiyear ice dominant in 2005 that is thicker and not easily broken into smaller pieces, as smaller floes may reduce the pond coverage by producing shorter and more drainage paths for ponds into adjacent leads. The 2005 cruise was also ∼ 20 days later in timing. Different weather conditions might also have played a role in surface melting in the two years.

5.2 The increased bottom melt rate

In this study, the average 2 cm day^{-1} melt rate, primarily bottom melt, during the 12-day ice station (∼ 86°50′ N–87°20′ N), is larger than the average ∼ 0.8 cm day^{-1} during the similar period (early to mid-August) of SHEBA experiments in 1998, even though SHEBA was at much lower latitudes (70–80° N) (Perovich et al., 2003). The average bottom melt in the 1998 melt season of the SHEBA experiment was 62 cm, which was more than twice the amount from previous reports of 1957–1994 (Perovich et al., 2003; Eicken et al., 2004). This might suggest that change has happened in the Arctic sea ice since 1998. Specifically, the increased solar heating (500 % positive anomaly) to the upper ocean was the primary reason for the high bottom melt rate in the Beaufort sea (2.1 m) in 2007, which was 6 times more than the annual mean (0.34 m) in the 1990s and 2.5 times more than that in 2006 (Perovich et al., 2008). In the month of August 2007, the mean bottom melt rate in Beaufort Sea (∼ 76° N) was 4 cm per day (up to 11 cm per day in the last week of August), five times larger than the average 0.8 cm day^{-1} in the same region in 1998 (Perovich et al., 2003). The significant increase in solar heating in 2007 was primarily due to increased open water area (51 %) in 2007 from the mean value (26 %) between 1979–2005.

In contrast, in the 12-day drift station of this study, the floe was so big (over 100 km^2 in size and ∼ 1.8 m in mean thickness) and was far north (more than 1000 km away) from the ice edge. Therefore, a large open water induced solar heating should be very limited. Based on airborne surveys and AMSR-E data (not shown), the ice concentration in the central Arctic ocean in later July to August 2010 period was low (around 70–80 %). We can then approximately calculate the solar heat contribution for the bottom ice melting using Eq. (3) (Hobbs, 1974).

$$\Delta z = \frac{E_0 \tau}{\rho_i L} [C_0(1-\alpha_i) + (1-C_0)(1-\alpha_w)], \quad (3)$$

where Δz is the maximum potential ice melt rate per day (m day^{-1}); τ is the seconds per day (86 400); ρ_i (kg m^{-3}) is sea ice density; L (J kg^{-1}) is sea ice latent heat of fusion; and E_0 (W m^{-2}) is the solar heat flux to the surface, which is partly absorbed by ice and water, with C_0 for ice concentration, α_i for sea ice albedo and α_w for open water albedo (usually 0.05).

Based on field-measured data for the drift station period (8–19 August), the daily mean downward solar heat flux varied from 97 W m^{-2} to 158 W m^{-2} (mean 122 W m^{-2}) and the ice albedo varied from 0.61 to 0.79 (mean 0.75). The ice density is taken as 845 kg m^{-3} (from 839 kg m^{-3} to 851 kg m^{-3}) (Lei et al., 2012). L is taken as 297 783 J kg^{-1}, based on the equation (Ono, 1968), $L = 333\,394 - 2113\,T - 114.2\,S + 18040\,(S/T)$, where T is the measured sea ice temperature (−0.58 °C) and S is the bulk salinity (1.18 PSU), both values from Lei et al. (2012). Therefore, the resultant melt rate Δz could be from 0.013 to 0.023 m day^{-1} (mean 1.6 cm day^{-1}), given ice concentration 80 %, and 0.015–0.026 m day^{-1} (mean 1.9 cm day^{-1}), given ice concentration 70 %. These rates were the maximum potential ice melt rates under the assumption that all the absorbed solar radiation was used for bottom melt of sea ice and were very close the 2 cm day^{-1} measured by EM-31 instruments.

An additional source of heat contributing to the high bottom melt rate could be due to the high drift speed. Drift speed is a proxy for turbulent mixing (Perovich et al., 2003) and increased drift speed probably played a major role for the increased bottom melt rate in the Arctic Transpolar Drift in 2007 (Nicolaus et al., 2010). The 12-day station (from 7–19 August) in this study, started at 86.92° N,178.88° W and drifted a total of 181 km, at a rate of 0.17 ± 0.08 m s^{-1} (Fig. 11). Rampal et al. (2009) examined the International Arctic Buoy Program (IABP) data from 1979 to 2007 and showed acceleration in drift speed; particularly, an 8.5 % increase per decade for summer seasonal mean (e.g., 0.08 m s^{-1} to 0.09 m s^{-1} from 1979 to 2007), so the drift rate at the time of measurement (0.17 m s^{-1}) was approximately twice the 2007 mean (0.09 m s^{-1}). As indicated in McPhee et al. (2003, 2008), the ocean–ice heat flux can be very well parameterized as a function of departure

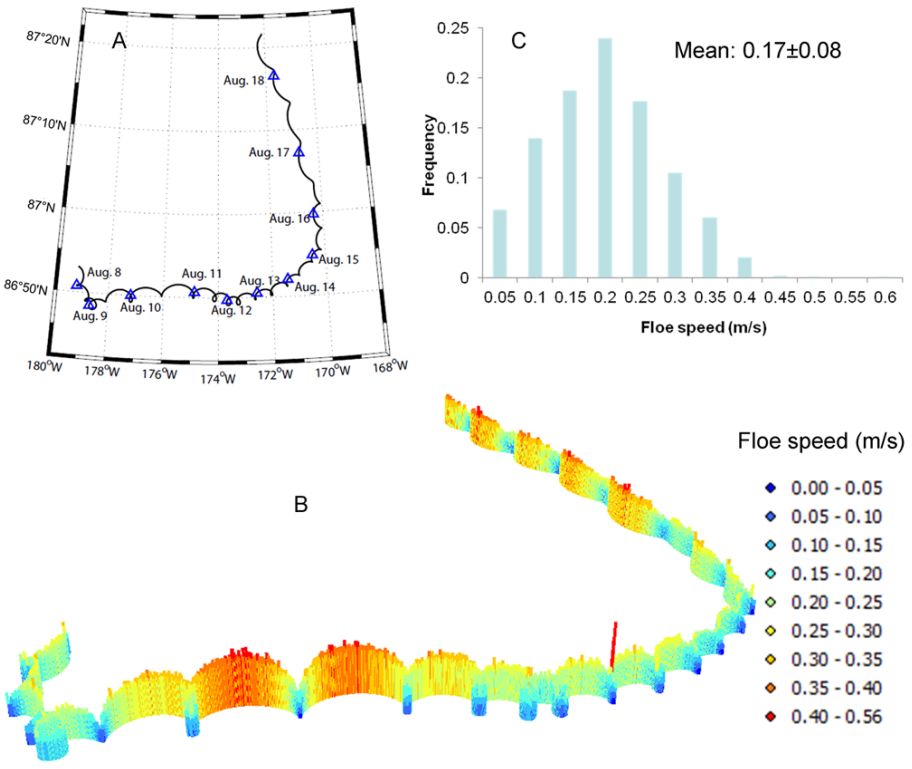

Fig. 11. Floe drift track **(A)**, floe speed in 3-dimensional view **(B)**, and floe speed distribution **(C)** during the 12-day ice station.

from freezing and friction speed (closely related to floe drift speed).

5.3 Visual observations and automated data collection

Although there are large differences in terms of sampling frequency and area between the half-hourly visual observations (2 km diameter) and the one-second interval of EM31 thickness measurements (footprint 13 m, 3.7 times the instrument altitude 3.5 m, Reid et al., 2006), the information provided shows general agreement. Based on literature (Hass et al., 2010), the EM31 are most accurate with respect to their modal thickness, which is consistent with that seen from our visual observations, i.e., the thickness of the dominant ice type. As shown in Fig. 6, the highest modal thicknesses (160 cm for northward leg and 140 cm for the southward leg) match well with the corresponding visual observations (150 cm and 130 cm, respectively). The differences between the two are partly due to the snow depth that was part of the EM31 thickness but was not added into the ice thickness of visual observations, as well as errors from both the instrument and visual observations. For most of the ice observations, there was no snow on the ice, except for the period 1–8 August when there were new snowfall events (6–10 cm snow) and both EM31 data and ice observations were available. Adding the 6–10 cm snow into the observed snow and ice thickness would only change the statistics a few centimeters. Therefore, this comparison shows that the modal thickness from visual observations is a reasonable modal thickness for the dominant ice type. The large footprint of 13 m of the EM31 can also help explain the 10 cm modal thickness from the EM31 for both legs (Fig. 6), since we did not remove those footprints (or noise) when the ship moved in leads or open water, as well as footprints of mixed water and ice that generally could have thicknesses of 20 cm and 30 cm. The 40 cm (snow and ice thickness) in the southward leg (EM31) seems to match well with the 30 cm modal thickness (ice only) from visual observations (Fig. 6d). As for errors in EM31, based on SIMBA measurements in the Antarctic (Weissling et al., 2011), the error of in situ EM measurements was < 10 % (root mean squared error) for level ice. This is similar to the Arctic case we obtained from this study during the 12-day ice station period (3–7 %). Haas et al. (2008) and Pfaffling et al. (2007) showed the airborne EM has an accuracy of ± 10 cm for level ice but can be less than 50 % of the true thickness for unconsolidated ridges.

While both EM31 and visual observations provide similar and compatible modal thickness, the EM31 provides more detailed information on ice thickness and its change without possible interruption or human-induced error. Visual observations compared with EM31 measurements are massively undersampled, i.e., 166 (visual) vs 58 563 (EM31) for the northward leg and 120 (visual) vs 103 107 (EM31) for the southward leg (Fig. 6). There are also significant differences

on maximum ice thickness measured by EM31 (i.e., 902 cm) and often not reported by visual observations. Note that the ship-based EM31 (3.5 m above waterline) was struck three times by isolated thick floebergs during the entire cruise (Fig. 2c shows a floeberg 10 m in diameter and over 4 m above the sea surface with estimated thickness > 10 m on 26 August that was struck by the hanging EM31).

The utility of the ship-based ice thickness observations, if used directly to compare with EM31 values, is to provide the modal ice thickness for the dominant ice type (i.e., the highest ice concentration or fraction of ice type). Worby et al. (2008), however, calculate a mean total ice thickness based on fractions of the ice types and ridges. Therefore, the ASPeCt mean thickness based on the method from Worby et al. (2008) is not compatible with the modal thickness from ship-mounted EM31 measurements. Instead, the corresponding term in the ASPeCt observations is the "level ice thickness" of the highest concentration ice type, which provides the comparative modal thickness for the dominant ice type compared to the observations reported here.

Together the visual observations and ship-based EM31 provide significant and independent measurements of ice physical properties, and are equally important and needed. Data acquired from EM31 are also more robust and can be reanalyzed, in contrast with visual observations that do not allow later revisiting and correction of scenes. It is impossible to recheck if there is any bias or inconsistency due to different experiences from observer to observer. In addition, the EM31 provides systematic datasets better suited to quantitative analyses as compared with the visual observations, with possible biases from different observers and from different cruises leading to uncertainty in their identification of change. The high density of sampling from an automated EM31 system is invaluable and should be performed for any and each ship opportunity to the polar regions, particularly with the current lack of satellite lidar with the demise of ICESat.

6 Summary and conclusions

This paper presents results from ship-based visual observations of ice concentration, ice thickness, snow thickness, floe size, and melt pond coverage half hourly, as well as higher frequency (1/s) automated EM31 measurements of ice thickness, over the Arctic Pacific sector during the CHINARE-2010, primarily during the period of 21 July to 28 August. The combined information from all those data provide a broad perspective of the sea ice cover with respect to its spatial and temporal variations over the Pacific Arctic sector for the study period. This invaluable dataset can be used for comparison with previous data or as a benchmark for future change. Modal thickness from ship-based visual observations matches well with the largest modal thickness from the ship-based EM31 along the cruise track. The latter provides systematic datasets better suited to quantitative analyses as compared with the visual observations that may be biased between different observers and from different cruises leading to uncertainty in their identification of change.

Besides the obvious difference in ice concentration between the pack ice zone and the marginal ice zone (MIZ), there are clear differences in ice thickness, ice type, floe size, and pond coverage. We summarize those parameters in the MIZ of the 2010 cruise as the following: (1) The ice thickness of the dominant ice type was 100 cm in late July (northward leg) and thinned to less than 50 cm in later August (southward leg); (2) ice type was either thick first-year ice or multi-year ice, with a higher fraction of dirty ice for the northward leg, while it seems the same type of ice was observed, but much thinner, in the southward leg; (3) floe size was typically 2–100 m; and (4) melt pond coverage was 16 % for the northward leg and 10 % for the southward leg.

An 8-profile grid of ice thickness measurements (four repeats) was conducted in the heart of the Central Arctic Ocean and an average 2 cm day^{-1} melt rate, primarily bottom melt, is found. The design of such a grid enables us to do a sea ice thickness study, by producing an ice thickness map of a sizable area and to study the changes over time using repeated measurements. This type of dataset would be even more valuable for calibration and/or validation purposes, if simultaneous airborne or satellite measurements of ice thickness can be made contemporaneously.

Acknowledgements. The study was partially supported by the NASA grant (#NNX08AQ87G), the Chinese NSF grant (#40930848), the National High Technology Research and Development Program of China (#2010AA09Z103) and the Oversea Cooperation Program of Chinese Arctic and Antarctic Administration (#IC201301). Travel expenses for H. Xie for the cruise were covered by NOAA's Climate Research/Sea Ice Outlook Program. We sincerely acknowledge the support from the Chinese Arctic and Antarctic Administration, the Chinese Arctic Expedition Team-2010, and the other persons of the sea ice team of the cruise. Advice from Christian Haas and Blake Weissling for processing the EM31 data and critical reviews from two anonymous reviewers and Hajo Eicken, Editor, to improve the paper are all greatly appreciated.

Edited by: H. Eicken

References

Boetius, A., Albrecht, S., Bakker, K., Bienhold, C., Felden, J., Fernández-Méndez, M., Hendricks, S., Katlein, C., Lalande, C., Krumpen, T., Nicolaus, M., Peeken, I., Rabe, B., Rogacheva, A., Rybakova, E., Somavilla, R., Wenzhöfer, F., and RV *Polarstern* ARK27-3-Shipboard Science Party.: Export of algal biomass from the melting Arctic sea ice, Science, 339, 1430–32, 2013.

Comiso, J. and Nishio, F.: Trends in the sea ice cover using enhanced and compatible AMSR-E SSM/I and SMMR

Data. Journal of Geophysical Research 113, C02S07, doi:10.1029/2007JC004257, 2008.

Darby, D. A., Myers, W. B., Jakobsson, M., and Rigor, I.: Modern dirty sea ice characteristics and sources: The role of anchor ice, J. Geophys. Res., 116, C09008, doi:10.1029/2010JC006675, 2011.

Eicken, H., Grenfell, T. C., Perovich, D. K., and Richter-Menge, J. A., and Frey, K.: Hydraulic controls of summer Arctic pack ice albedo. J. Geophys. Res., 109, C08007, doi:10.1029/2003JC001989, 2004.

Eicken, H., Gradinger, R., Gaylord, A., Mahoney, A., Rigor, I., and Melling, H.: Sediment transport by sea ice in the Chukchi and Beaufort Seas: Increasing importance due to changing ice conditions?, Deep Sea Res. Pt. II, 52, 3281–3302, 2005.

Hass, C. and Druckenmiller, M.: Ice thickness and roughness measurements, in Field Techniques for Sea Ice Research, edited by: Eicken, H. and Salganek, M., 565 pp., University of Alaska Press, 2009.

Haas, C., Pfaffling, A., Hendricks, S., Rabenstein, L., Etienne, J. L., and Rigor, I.: Reduced ice thickness in Arctic Transpolar Drift favors rapid ice retreat, Geophys. Res. Lett., 35, L17501, doi:10.1029/2008GL034457, 2008.

Haas, C., Hendricks, S., Eicken, H., and Herber, A.: Synoptic airborne thickness surveys reveal state of Arctic sea ice cover, Geophys. Res. Lett., 37, L09501, doi:10.1029/2010GL042652, 2010.

Hobbs, P. V.: Ice, Physics, Clarendon Press, Oxford, p. 837, 1974.

Intergovernmental Panel on Climate Change (IPCC): Climate Change 2007: The Physical Science Basis, Contribution of Working Group I to the Fourth Assessment Report of the Intergovernmental Panel on Climate Change, edited by: Solomon, S., Qin, D., Manning, M., Chen, Z., Marquis, M., Averyt, K. B., Tignor, M., and Miller, H. L., Cambridge Univ. Press, Cambridge, UK, 2007.

Itoh, M., Inoue, J., Shimada, K., Zimmermann, S., Kikuchi, T., Hutchings, J., McLaughlin, F., and Carmack, E.: Acceleration of sea-ice metling due to transmission of solar radiation through ponded ice area in the Arctic Ocean: results of in situ observations from icebreakers in 2006 and 2007, Ann. Glaciol., 52, 249–260, 2011.

Kwok, R.: Satellite remote sensing of sea ice thickness and kinematics: A review, J. Glaciol., 56, 1129–1140 2011.

Kwok, R. and Rothrock, D. A.: Decline in Arctic sea ice thickness from submarine and ICESat records: 1958–2008, Geophys. Res. Lett., 36, L15501, doi:10.1029/2009GL039035, 2009.

Kwok, R. and Untersteiner, N.: The thinning of Arctic sea ice, Phys. Today, 64, 36–41, 2011.

Kempema, E. W., Reimnitz, E., and Barnes, P. W.: Sea ice sediment entrainment and rafting in the Arctic, J. Sediment. Petrol., 59, 308–317, 1989.

Leppäranta, M.: The Drift of Sea Ice, ISBN 3-540-40881-9, Springer-Praxis Books in Geophysical Sciences, Chichester, UK, 266 pp., 2005.

Lei, R., Zhang, Z., Matero I., Cheng, B., Li, Q., and Huang, W.: Reflection and transmission of irradiance by snow and sea ice in the central Arctic Ocean in summer 2010, Polar Res., 31, 17325, doi:10.3402/polar.v31i0.17325, 2012.

Lu, P., Li, Z., Cheng, B., Lei, R., and Zhang, R.: Sea ice surface features in Arctic summer 2008: Aerial observations, Remote Sens. Environ., 114, 693–699, doi:10.1016/j.rse.2009.11.009, 2010.

Maslanik, J. A., Fowler, C., Stroeve, J., Drobot, S., Zwally, J., Yi, D., and Emery, W.: A younger, thinner Arctic ice cover: Increased potential for rapid, extensive sea-ice loss, Geophys. Res. Lett., 34, L24501, doi:10.1029/2007GL032043, 2007.

McPhee, M. G., Kikuchi, T., Morison, J. H., and Stanton, T. P.: Ocean-to-ice heat flux at the North Pole environmental observatory, Geophys. Res. Lett., 30, 2274, doi:10.1029/2003GL018580, 2003.

McPhee, M., Morison, J. H., and Nilsen, F.: Revisiting heat and salt exchange at the ice-ocean interface: Ocean flux and modeling considerations, J. Geophys. Res., 113, C06014, doi:10.1029/2007JC004383, 2008.

Nghiem, S. V., Rigor, I. G., Perovich, D. K., and Clemente-Colon, P.: Weatherly, J. W., and Neumann, G.: Rapid reduction of Arctic perennial sea ice, Geophys. Res. Lett., 34, L19504, doi:10.1029/2007GL031138, 2007.

Nicolaus, M., Gerland, S., Hudson, S. R., Hanson, S., Haapala, J., and Perovich, D. K.: Seasonality of spectral albedo and transmittance as observed in the Arctic Transpolar Drift in 2007, J. Geophys. Res., 115, C11011, doi:10.1029/2009JC006074, 2010.

Ono, N.: Thermal properties of sea ice, IV. Thermal constants of sea ice, Low Temp. Sci., Ser. A, 26, 329–349, 1968.

Perovich, D. K.: The changing Arctic sea ice cover, Oceanography, 24, 162–173, doi:10.5670/oceanog.2011.68, 2011.

Perovich, D. K., Grenfell, T. C., Light, B., and Hobbs, P. V.: Seasonal evolution of the albedo of multiyear Arctic sea ice, J. Geophys. Res., 107, 8044, doi:10.1029/2000JC000438, 2002.

Perovich, D. K., Grenfell, T. C., Richter-Menge, J. A., Light, B., Tucker III, W. B., and Eicken, H.: Thin and thinner: Sea ice mass balance measurements during SHEBA, J. Geophys. Res., 108, 8050, doi:10.1029/2001JC001079, 2003.

Perovich, D. K., Richter-Menge, J. A., Jones, K. F., and Light, B.: Sunlight, water, and ice: Extreme Arctic sea ice melt during the summer of 2007, Geophys. Res. Lett., 35, L11501, doi:10.1029/2008GL034007, 2008.

Perovich, D. K., Grenfell, T. C., Light, B., Elder, B.C., Harbeck, J., Polashenski, C., Tucker III, W. B., and Stelmach, C.: Transpolar observations of the morphological properties of Arctic sea ice, J. Geophys. Res., 114, C00A04, doi:10.1029/2008JC004892, 2009.

Pfaffling, A., Haas, C., and Reid, J. E.: A direct helicopter EM sea ice thickness inversion, assessed with synthetic and field data, Geophysics, 72, 127–137, 2007.

Rabenstein, L., Hendricks, S., Martin, T., Pfaffhuber, A., and Haas, C.: Thickness and surface-properties of different sea-ice regimes within the Arctic Trans Polar Drift: Data from summers 2001, 2004 and 2007, J. Geophys. Res., 115, C12059, doi:10.1029/2009JC005846, 2010.

Rampal, P., Weiss, J., and Marsan, D.: Positive trend in the mean speed and deformation rate of Arctic sea ice, 1979–2007, J. Geophys. Res., 114, C05013, doi:10.1029/2008JC005066, 2009.

Reid, J. E., Pfaffling, A., and Vrbancich, J.: Airborne electromagnetic footprints in 1D earths, Geophysics, 71, G63–G72, doi:10.1190/1.2187756, 2006.

Serreze, M. C., Barrett, A. P., Slater, A. G., Steele, M., Zhang, J., and Trenberth, K. E.: The large-scale energy budget of the Arctic, J. Geophys. Res., 112, D11122, doi:10.1029/2006JD008230, 2007.

Simmonds, I. and Keay, K.: Extraordinary September Arctic sea ice reductions and their relationships with storm behavior over 1979–2008, Geophys. Res. Lett., 36, L19715, doi:10.1029/2009GL039810, 2009.

Squire, V. A.: Of ocean waves and sea-ice revisited, Cold Reg. Sci. Technol., 49, 110–133, 2007.

Steele, M.: Sea ice melting and floe geometry in a simple ice-ocean model, J. Geophys. Res., 94, 17729–17738, 1992.

Stroeve, J., Holl, M., Meier, W., Scambos, T., and Serreze, M.: Arctic sea ice decline: Faster than forecast, Geophys. Res. Lett., 34, L09501, doi:10.1029/2007GL029703, 2007.

Toyota, T., Kawamura, T., Kay, I. O., Shimoda, H., and Wakatsuchi, M.: Thickness distribution, texture and stratigraphy, and a simple probabilistic model for dynamical thickening of sea ice in the southern Sea of Okhotsk, J. Geophys. Res., 109, C06001, doi:10.1029/2003JC002090, 2004.

Wang, J., Guo, J., Wang, H., Sun, B. and Tian, G.: Data analysis of shipborne EM31-ice measurmening in China's fourth Arctic scientific expedition, Chinese Journal of Polar Research, 24, 47–52, doi:10.3724/SP.J.1084.2012.00047, 2012.

Wang, X., Xie, H., Ke, Y., Ackley, S. F., and Liu, L.: A method to automatically determine sea level for referencing snow freeboards and computing sea ice thicknesses from NASA IceBridge airborne LIDAR, Remote Sens. Environ., 131, 160–172, doi:10.1016/j.rse.2012.12.022, 2013.

Weissling, B., Lewis, M. J., and Ackley, S. F.: Sea ice thickness and mass at Ice Station Belgica, Bellingshausen Sea, Antarctica, Deep Sea Res. Pt. II, 58, 1112–1124, doi:10.1016/j.dsr2.2010.10.032, 2011.

Worby, A. P. and Allison, I.: A technique for making ship-based observations of Antarctic sea ice thickness and characteristics, Part I: Observational technique and results, Antarctic CRC Research Report 14, 1–23, 1999.

Worby, A. P., Geiger, C., Paget, M., Van Woert, M., Ackley, S., and DeLiberty, T.: Thickness distribution of Antarctic Sea Ice, J. Geophys. Res., 113, C05S92, doi:10.1029/2007JC004254, 2008.

Xie, H., Ackley, S. F., Yi, D., Zwally, H.J., Wagner, P., Weissling, B., Lewis, M., and Ye, K.: Sea ice thickness distribution of the Bellingshausen Sea from surface measurements and ICESat altimetry, Deep Sea Res. Pt. II, 58, 1039–1051, doi:10.1016/j.dsr2.2010.10.038, 2011.

Xie, H., Tekeli, A. E., Ackley, S. F., Yi, D., and Zwally, H. J.: Sea ice thickness estimations from ICESat altimetry over the Bellingshausen and Amundsen Seas, 2003–2009, J. Geophys. Res., 118, 1–16, doi:10.1002/jgrc.20179, 2013.

Zwally, H. J., Schutz, B., Abdalati, W., Abshire, J., Bentley, C., Brenner, A., Bufton, J., Dezio, J., Hancock, D., Harding, D., Herring, T., Minster, B., Quinn, K, Palm, S., Spinhirne, J. and Thomas, R.: ICESat's laser measurements of polar ice, atmosphere, ocean, and land, J. Geodyn., 34, 405–445, 2002.

Zwally, H. J., Yi, D., Kwok, R., and Zhao, Y.: ICESat measurements of sea ice freeboard and estimates of sea ice thickness in the Weddell Sea, J. Geophys. Res., 113, C02S15, doi:10.1029/2007JC004284, 2008.